Detection of melamine on fractals of unmodified gold nanoparticles by surface-enhanced Raman scattering

Pradip Kumar Roy
Yi-Fan Huang
Surojit Chattopadhyay

Detection of melamine on fractals of unmodified gold nanoparticles by surface-enhanced Raman scattering

Pradip Kumar Roy,[a] **Yi-Fan Huang,**[a] **and Surojit Chattopadhyay**[a,b]
[a]National Yang-Ming University, Institute of Biophotonics, Taipei 112, Taiwan
[b]National Yang Ming University, Biophotonics and Molecular Imaging Research Centre, Taipei-112, Taiwan

Abstract. A simple way of detecting melamine in raw milk is demonstrated via surface-enhanced Raman spectroscopy (SERS) using fractals of bare and nonfunctionalized ~30 nm gold nanoparticles (AuNP) distributed on a solid support. The technique demonstrates the formation of AuNP fractals, from a random distribution, upon exposure to melamine, that enhance the Raman scattering cross-section to enable detection by SERS. The agglomeration, which is pronounced at higher melamine concentrations, is demonstrated directly through imaging, and the red-shift of the plasmon absorption peak of the AuNP fractal away from 530 nm by finite difference time domain (FDTD) calculations. The agglomeration results in a strong plasmon field, shown by FDTD, over the interparticle sites that enhances the Raman scattering cross-section of melamine and ensures unambiguous detection. Limit of detection of 100 ppb could be achieved reproducibly. © *2014 Society of Photo-Optical Instrumentation Engineers (SPIE)* [DOI: 10.1117/1.JBO.19.1.011002]

1 Introduction

1,3,5-triazine-2,4,6-triamine commercially known as melamine, $C_3H_6N_6$, is generally used in laminates, coatings, or glass wares as melamine formaldehyde resins. However, the high nitrogen content (66% by mass), lured unreliable manufacturers to use it to fake the protein content, indicated by nitrogen, in infant milk formula and petfood. Melamine and cyanuric acid, or any other melamine related compounds such as ammeline, ammelide, and 1-(2-mercaptoethyl)-1,3,5-triazinane-2,4,6 trione (MTT),[1–3] may produce complexes in the human body[4–6] when they combine together via hydrogen bonds. At higher concentrations (more than 1 ppm/day for child and 3 ppm/day for adult) those complexes will aggregate in the kidneys and form kidney stones[4,5,7] causing urinary system inflammation[4,5] or urolithiasis. The World Health Organization (WHO) estimated the "tolerable daily intake," to be 0.2°mg per kg of body mass.[8] Such toxic additives have to be detected quickly and mass production of food items has to be controlled by authorities.

This calls for reliable and accurate sensing techniques and materials with reasonable ease-of-use. Conventionally, melamine is detected by high performance liquid chromatography (HPLC),[9,10] liquid chromatography coupled mass spectroscopy (LC-MS),[11] LC-MS/MS, gas chromatography,[9,12,13] matrix assisted laser desorption/ionization mass spectrometry,[14] variety of ionization mass spectrometry,[15,16] commercial enzyme linked immunosorbent assay technology,[17] and infrared spectroscopy.[18] These laboratory-based techniques, although reliable and accurate, are time consuming, and challenging for on-site common use. Relatively easier methods include optical absorption[19–23] and Raman spectroscopy (RS), including surface-enhanced Raman spectroscopy (SERS).[24–27] Recently, optical absorption

studies are being used to detect melamine using MTT functionalized gold nanoparticles (AuNP).[22] MTT attaches at one end to the AuNPs, by the thiol bond, and upon exposure to melamine bind to it through hydrogen bonding, thus agglomerating the AuNPs into clusters. The agglomeration will alter the surface plasmon absorption wavelength from 520 nm, for MTT stabilized AuNPs, to ~670 nm for the melamine exposed AuNPs. The shift, a function of melamine concentration, in this absorption frequency, observable by naked eye, is used for colorimetric sensing of melamine. However, such studies always used functionalized or modified AuNPs. Similar colorimetric determination of the presence of melamine can be done using Fe_3O_4 magnetic NPs with 2.5 ppm detection levels.[23] Recently, SERS is also being used for the sensing purpose.[24] For SERS noble metal (Au, Ag) NP decorated substrates were used to enhance the scattering cross-section of melamine and hence lowering the detection limit. SERS is a technique that can be used on-site with relatively smaller degree of difficulty.

In the present work, we demonstrate how the target analyte, melamine, itself induces agglomeration in unmodified gold nanoparticles, resulting in fractals on solid support in air, enabling target detection by SERS. Using finite difference time domain (FDTD) optical simulation we provide a preferred condition of plasmon distribution on the Au-fractal substrate that would be necessary for the sensing.

2 Experimental

2.1 Synthesis of Gold Nanoparticles

AuNPs were prepared by the conventional wet chemical method reducing a 10 mMchloroauric acid ($HAuCl_4$) (ACROS-411070010) solution, in DI water, with 1% trisodium citrate ($Na3C6H5O7$, ACROS-227130010) at 100°C.[28,29] The reducing

Address all correspondence to: Surojit Chattopadhyay, 155, Section-2, Li-Nong Street, Taipei-112, Taiwan. Tel: + 886 2 2826 7909; Fax: + 886 2 2823 5460; E-mail: sur@ym.edu.tw

agent and its concentration is the main ingredient controlling the resultant AuNPs size. A colloidal solution of AuNPs in water is thus obtained.

2.2 *Melamine Contaminated Water and Milk Sample Extraction*

Aqueous solutions of melamine were obtained by adding calculated amounts of melamine in DI water to attain target concentrations. These solutions were used for the AuNP fractal generation when dispersed on AuNP coated silicon surface. Melamine containing milk extracts were derived by mixing calculated amounts of melamine to commercial liquid milk to achieve concentrations (M_c) of 10, 1, 0.1, and 0.01 ppm concentrations, and then using citric acid to separate the protein in an ultra-centrifuge working at 10000 revolutions per minute, and collecting the supernatant. Proteins and fat components are removed for collection of the melamine contaminated supernatant. This will remove any effect of milk composition on the AuNPs.

2.3 *Instrumentation*

Optical images of the AuNPs colloid was taken with a Canon 7d (Japan) camera equipped with a 17 to 50 mm, f 2.8, Sigma lens. The AuNPs are characterized by transmission electron microscope (TEM, JEM-2000EX II, JEOL Corp., Japan) and high resolution scanning electron microscope (HRSEM, JEOL 5700F, Japan) for its size. The surface plasmon absorption peak of the AuNPs solution is measured by absorption spectroscopy using a double beam spectrophotometer (JASCO V-670, JASCO Corp., Japan). For accurate determination of the AuNPs size distribution, a dynamic light scattering (DLS) Nanosizer (Zetasizer Nano ZS90, Malvern Instruments Ltd. UK) was used. This machine is equipped with a 4 mW He-Ne laser (632.8 nm) and a temperature controller from 0°C to 90°C.

The Raman spectra were obtained using a commercial Jobin Yvon LabRAM HR800 (HORIBA Ltd., Japan) equipped with an Olympus BX-41 microscope and a liquid nitrogen cooled CCD detector. An excitation of 633nm laser was used. The spectral resolution of the machine was 0.6 cm^{-1}. The SERS substrates were prepared using standard crystalline
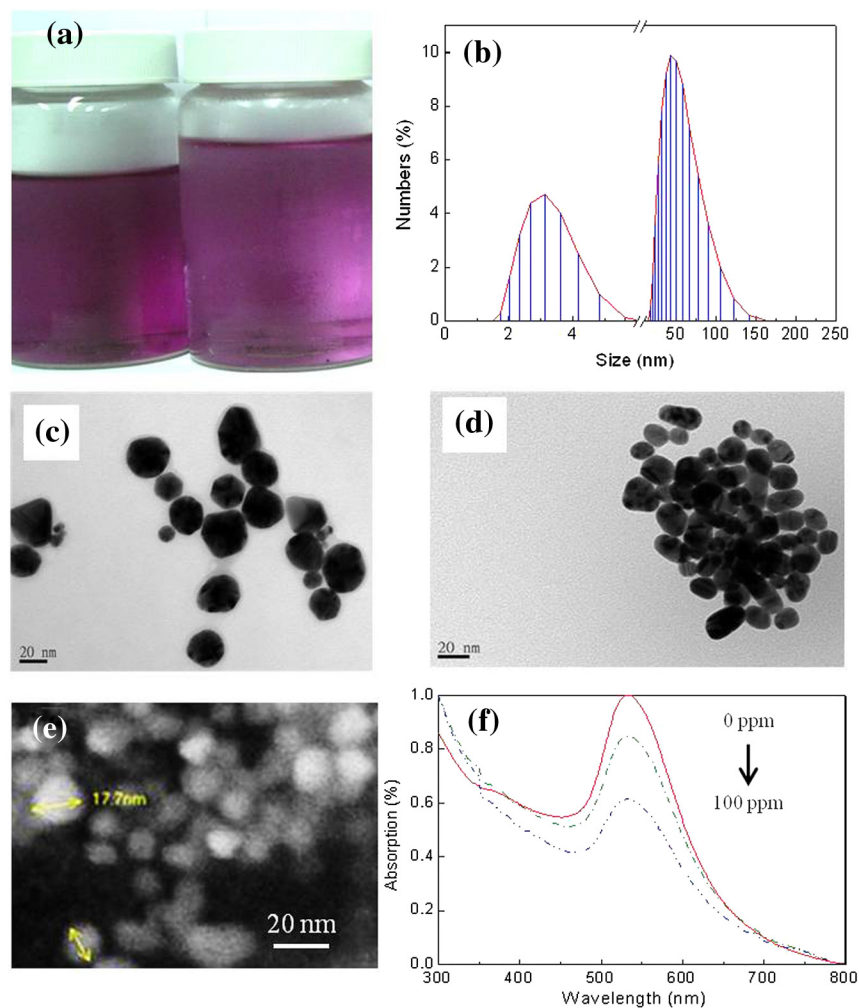
Fig. 1 Characterization of the colloidal gold nanoparticles (AuNPs). (a) A conventional optical photograph of the colloidal AuNPs. (b) The size distribution of the AuNPs. TEM image of the AuNPs (c) before, and (d) after 50 ppm melamine exposure. (e) SEM image of agglomerated AuNPs on Si after 50 ppm melamine exposure. (f) Optical absorption spectra, in colloidal solution, of the as-prepared AuNPs (0 ppm), and AuNPs exposed to 50 and 100 ppm of melamine.

silicon wafer on which 30 μL of the AuNPs solution was dispersed.

2.4 FDTD Simulation

Numerical simulations using the FDTD method (FDTD solutions, Version 7, Lumerical Solutions Inc., Canada) were performed to determine the role of the AuNPs size and interparticle distance on the resulting plasmonic properties of the as-dispersed and melamine induced agglomerated AuNPs. In order to mimic the experimentally obtained AuNPs distribution (before and after melamine introduction), a model for the FDTD simulation was developed by extracting the (x, y) coordinates of the AuNPs from a representative SEM top-view image. The model layout resembles the sectioned Au cluster, together with the particle size and interparticle separation, and introduced to the optical simulation software by the image import option. Simulation parameters include time step of 0.001 fs, mesh size of 1 nm (in all three directions, dx, dy, and dz), background index of 1.0, and 1.33, and known index of gold. Perfectly matched layer boundary conditions were used in all three directions.

3 Results and Discussion

For colorimetric[22,23] or Raman spectroscopic detection[24,30,31] of melamine, noble metal or magnetic NPs are generally used. In this case also we have used AuNPs, but without any cumbersome functionalization, for the detection using SERS. Figure 1 contains the details of the AuNP properties. The size control of AuNPs, prepared by the Turkevich method,[29] was achieved by varying the concentration of the reactants to obtain distinctive AuNP colloids with purple, red, and orange colors. An optical image of the AuNP colloid and its size distribution, measured by Zetasizer, is shown in Fig. 1(a) and 1(b), respectively. The particle size was predominantly in the 20 to 30 nm range with a distribution as expected of the Turkevich reaction.
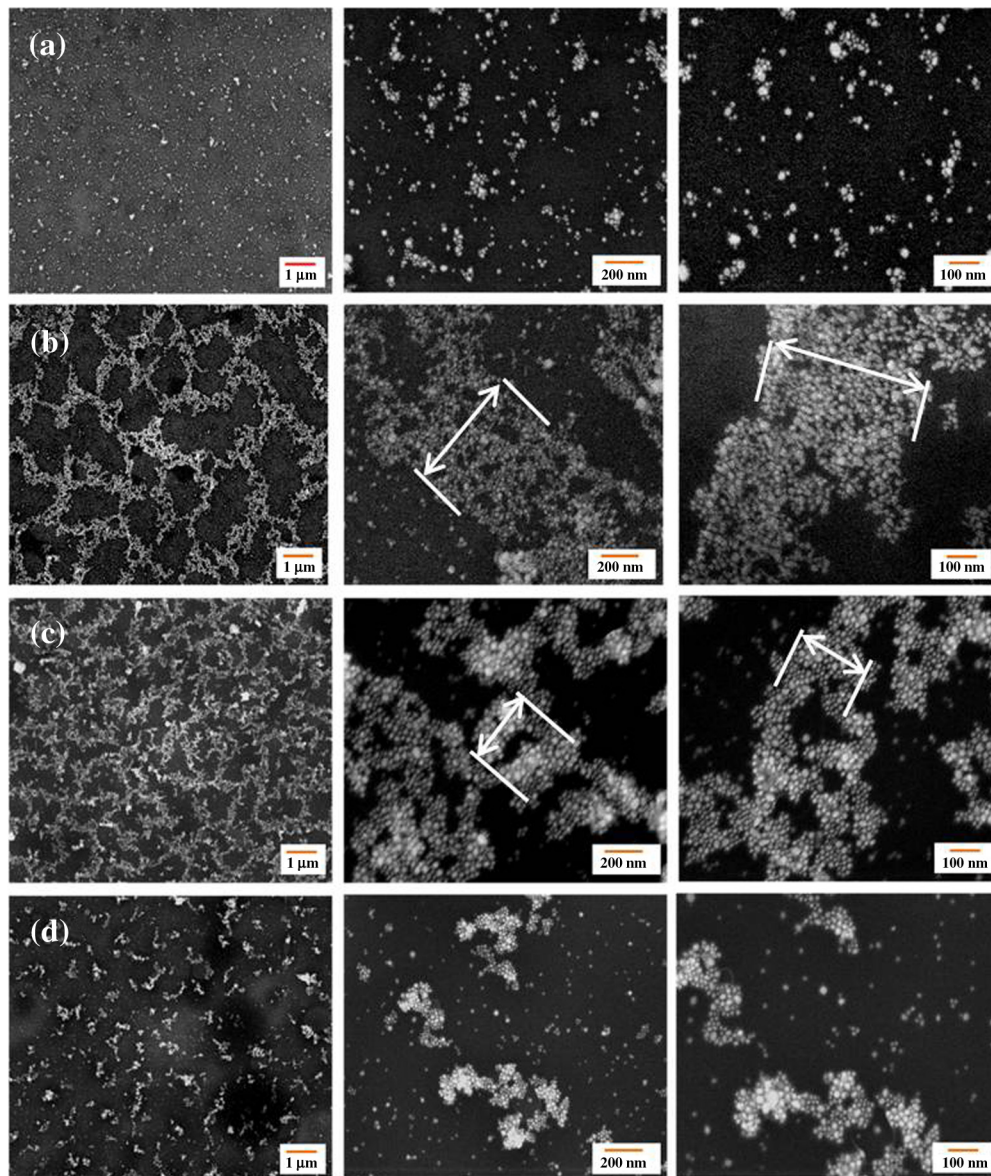
Fig. 2 Representative SEM images of (a) as-grown AuNPs, and the fractal-like AuNP clustering, on silicon, post melamine exposure of (b) 10, (c) 1, (d) 0.1 ppm. The left, middle, and right panel in each row contains images with 5000, 33000, and 50000 times magnification, respectively. The width of the AuNP chains or the fractal interconnects are shown in the (b) and (c) panels.

Representative TEM images of the AuNPs, on the TEM grid, as dispersed and after exposure to 50 ppm melamine is shown in Fig. 1(c), and 1(d), respectively. The AuNPs showed triangular and hexagonal features, and readily agglomerated upon exposure to melamine. Representative SEM image of the AuNPs after melamine exposure is shown in Fig. 1(e). Absorption spectra of the as-grown AuNP colloid, and those after addition of 50 and 100 ppm of melamine is shown in Fig. 1(f). The results showed a surface plasmon absorption peak at ∼530 nm. When

melamine with different M_c was added to the AuNP solution, the absorption peak intensity, at 530 nm, decreased [Fig. 1(f)] but no new peak, at higher wavelengths, found in the colorimetric detection methods, was observed that would imply significant agglomeration of the AuNPs in the solution. This is expected since the electrostatic repulsion of the Cl- surface coverage resisted the agglomeration. This is why MTT[22] or riboflavin[20] functionalization of the AuNPs was done. However, if sufficient amount of melamine is added (50 to 100 ppm) to the
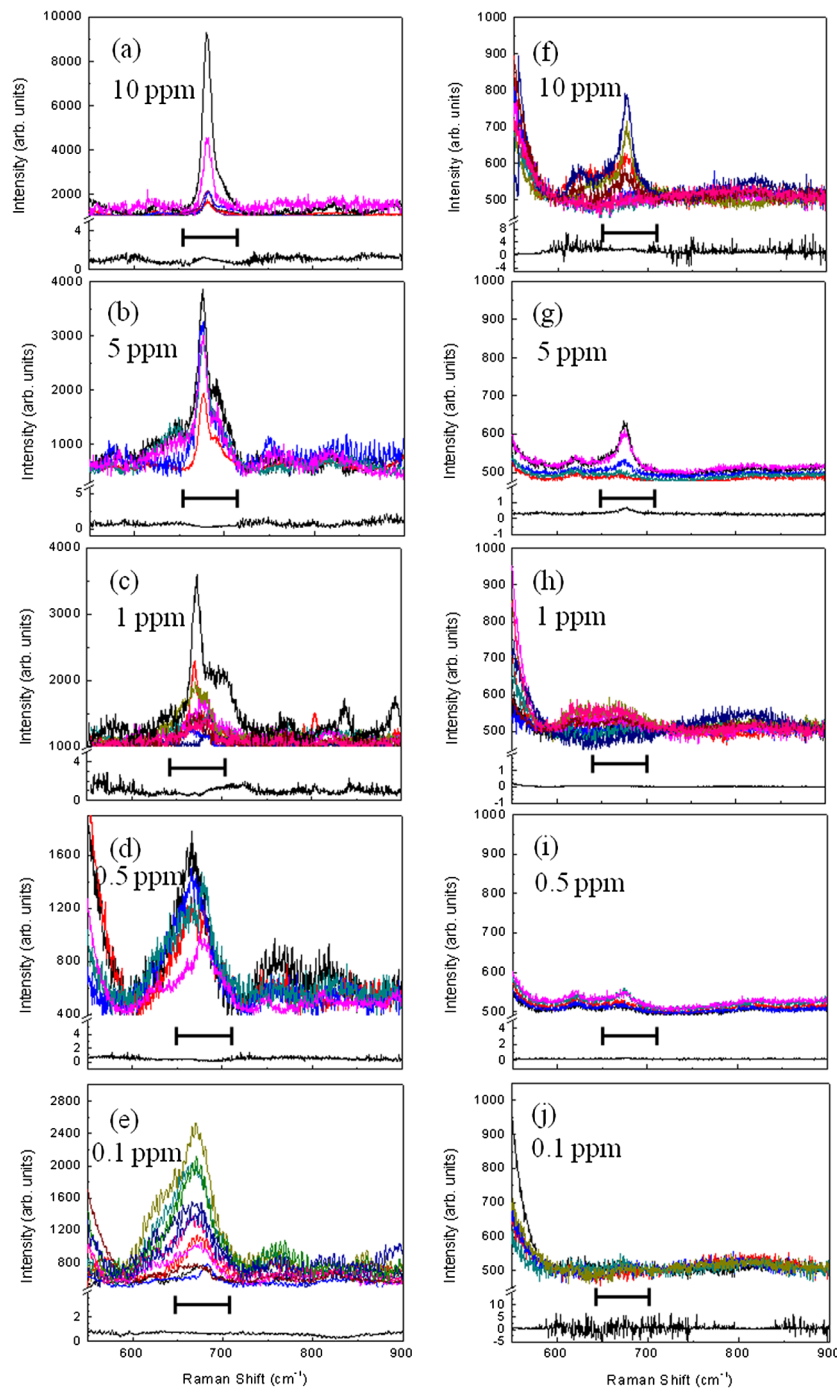
Fig. 3 Surface-enhanced Raman spectra (SERS), collected at 5 different spots of the same AuNP fractals, of melamine with (a) 10, (b) 5, (c) 1, (d) 0.5, and (e) 0.1 ppm concentration. Corresponding Raman spectra (RS) for melamine, on bare Si (non-SERS), with the same concentrations are shown in (f) to (j). The relative standard deviation (rsd) of the statistical data is shown at the bottom of each plot (before the scale break on the vertical axes). The spectra were shifted vertically for clarity. The spectral region of interest for melamine detection is marked by a horizontal bar in each figure.

AuNP solution such an agglomeration could be actually observed even in unmodified AuNPs but they are too weak to trigger the second peak at a higher wavelength. This proves that melamine have this inherent tendency to weakly agglomerate nonfunctionalized AuNPs even in solution.

The use of MTT[22] for AuNP agglomeration is prohibitive for three reasons. First, the production yield of MTT is low, secondly, its production cost is high, and lastly, it introduces an additional functionalization step in the whole detection process. Hence, our method aimed at discarding this step for the detection purpose. We tried to enhance the agglomeration effect on dry substrates that are devoid of the polar solvent, in this case, water. We dispersed 30 μL of the as-grown AuNPs on hydrofluoric acid (HF) cleaned commercial Si wafers and dried them in vacuum to get a clean two-dimensional (2-D) dispersion. Large population density of AuNPs is avoided (1) to restrict three-dimensional (3-D) clustering that would obstruct the agglomeration phenomenon, and (2) to simplify the optical simulations done to construct the plasmon distribution design (discussed later). There is no chemical bond between the Si substrate and the AuNPs covering it. Figure 2 contains SEM images of AuNPs before and after the exposure to different amounts of melamine. The as-dispersed AuNPs (dry), on Si in air, showed a density of 300 ± 30 NPs/μm^2 [Fig. 2(a)]. SEM was repeated [Fig. 2(a), all panels] at different magnifications and areas to verify the distribution that predominantly depended on the volume of the AuNPs solution and the wetting properties of the HF cleaned Si surface that showed a water contact angle of 43 deg at room temperature. Figure 2(b) to 2(d) showed the AuNPs distribution after exposure to 10, 1, and 0.1 ppm of melamine, respectively. As melamine is introduced, these AuNPs readily agglomerates forming an interconnected fractal-like network[32] leaving polygonal islands in between with less than 80 ± 20 NPs/μm^2 [Fig. 2(b) and 2(c)]. Such kind of fractal structures were previously obtained where a chain aggregate was constructed by sharing faces, corners, and edges of a polygon.[33,34] These edges, corners, or faces are the areas expected to have high SERS enhancement and ideal for melamine sensing that we would soon demonstrate. The peripheries of these islands are 400 to 600 nm thick containing chained and agglomerated AuNPs with a high 2-D spatial density approaching an ideal SERS enhancement condition[35] of $d = 2r$ where d is the interparticle separation and r is the radii of the AuNPs. In other words, the SERS efficiency is pronounced when AuNPs are nearly touching each other. The AuNP agglomeration was pronounced for $M_c = 10$ ppm, but the clustering weakens and the continuity of the fractal-network is broken as M_c is reduced to 0.1 ppm with the island boundaries thinning to ~100 nm when present at all [Fig. 2(d)]. In comparison, the AuNPs chains on the island boundaries were ~600 [Fig. 2(b)] and 350 nm [Fig. 2(c)] thick when 10 and 1 ppm of melamine was introduced, respectively.

The density of the AuNPs, counted manually by making 1 μm^2 meshes on 10 large area SEMs and neglecting meshes with fewer than 300 ± 30 NPs/μm^2 (as-dispersed density), were 2100 ± 100, 1450 ± 80, and 900 ± 50/μm^2 for exposures of $M_c = 10$, 1, and 0.1 ppm, respectively. In the large number of SEM images studied, we found very few 3-D clustering, which is not ruled out, but most of the melamine-induced agglomeration resulted in 2-D clustering under the given experimental conditions.
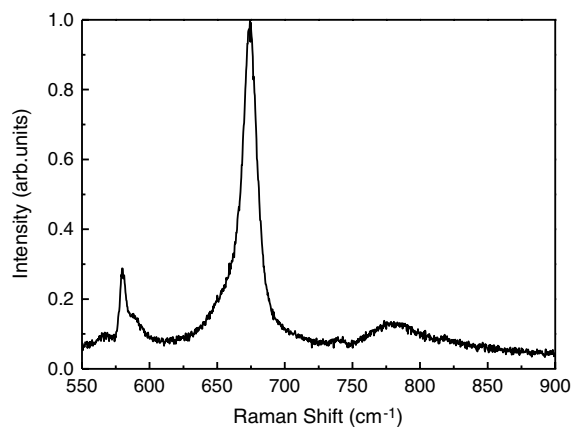
Fig. 4 Normalized Raman scattering data of melamine (bulk) powder, dispersed on Si, showing the signature peak at 676 cm^{-1}.

Figure 3(a) to 3(e) contain detailed SERS data of melamine (with $M_c = 10$, 5, 1, 0.5, and 0.1 ppm) dispersed on the AuNPs coated Si. For comparison, the RS data (not SERS) of melamine is shown for bare Si substrates (without the AuNPs) [Fig. 3(f) to 3(j)]. Spectra were obtained on different points on each substrate with a focus on the signature melamine (bulk) peak at 676 cm^{-1} (Fig. 4). Repeated scans and their relative standard deviations (rsd) are shown for each melamine concentration. To have a qualitative estimate of the efficacy of the AuNP-fractals in enhancing the signal, corresponding Raman data of melamine is provided on bare Si substrates [Fig. 3(f) to 3(j)] on which the 676 cm^{-1} signal was only visible for $M_c = 10$ and 5 ppm. The region of interest being around the strongest signal from melamine, 650 to 700 cm^{-1}, is marked in each plot in Fig. 3 scanned from 550 to 900 cm^{-1}. The 676 cm^{-1} signal (integrated area I$_{676}$) could be identified unambiguously down to the limit of 0.1 ppm [Fig. 3(e)] [with a signal: noise ratio (S/N) above 3:1] although its intensity decreased with decreasing M_c [Fig. 3(a) to 3(e)]. The rsd is used to estimate the repeatability (precision) of the measurements. Along different regions of the spectrum (550 to 900 cm^{-1}) the rsd varied between 10% to 30%, however, in the region of interest, 650
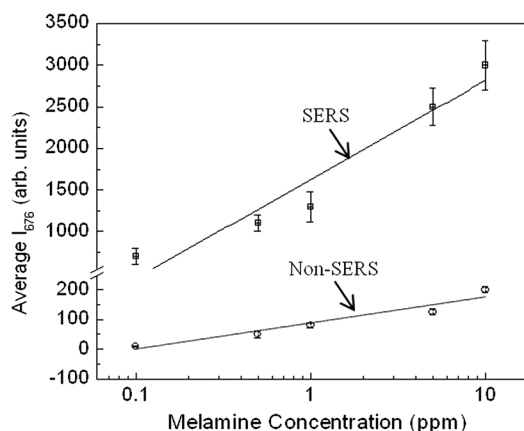
Fig. 5 Variation of the average intensity of the 676 cm^{-1} line of melamine Raman spectrum as a function of melamine concentration (in water, Fig. 3) when dispersed on (⊙) Silicon (non-SERS) and (⊕) gold fractals (SERS). A linear fit to the data is also shown. The R^2 values for the fitting are 0.9 and 0.92 for the SERS and non-SERS data set, respectively.

to 700 cm^{-1}, the rsd was <15% and flat indicating a small deviation of the signal intensity compared to other parts of the spectrum. The weak non-SERS spectra of melamine on bare Si substrates reveal qualitatively the efficacy of the AuNP-fractals in enhancing the signal.

The variation of the average I_{676} as a function of M_c is shown in Fig. 5, for both the SERS (on AuNP fractals) and non-SERS (reference plot, on bare silicon) cases. The slope of this plot (Fig. 5) is indicative of the sensitivity of detection in the studied concentration range. It is to be noted that the integrated signal intensity I_{676} is not only a function of M_c, but also a function of the number of SERS active sites (N_s) within the illuminated region (~12.5 μm^2) and with some simplifying assumptions we can write $I_{676} \propto N_s \times M_c$. One has to note that all AuNPs are not SERS active.[36] Given the increasing coverage (area) of AuNP clustering with M_c (Fig. 2), we expect an increase in N_s too, and hence a stronger I_{676} was observed [Fig. 3(a)]. In fact, Doering and Nie,[37] while comparing metallic single particle and aggregates for single molecule SERS, observed that the active sites or hot spots are most likely to be at the junction of two single particles in metallic aggregates. This supports our finding why the AuNP fractals helped in the detection.

It is difficult to estimate the SERS enhancement factor (EF = $\sigma_{SERS}/\sigma_{RS}$, σ being the Raman scattering cross-section) since the number of melamine molecules and N_s within the excited area, and the value of σ_{RS}, are all unknown.[38,39] However, with some approximation, a rough estimate of the EF can still be made using the following equation:[38,40]

$$\text{EF} = \frac{I_{SERS}}{I_{RS}} \times \frac{N_{bulk}}{N_{ads}},$$

where I_{SERS} and I_{RS} denote the signal strength of a particular Raman mode (676 cm^{-1}) of the analyte, melamine, in the presence of the AuNP fractals and on bare silicon, respectively. N_{bulk} and N_{ads} denote the number of melamine molecules, in the illuminated volume during Raman measurement, of bulk powder on bare silicon, and adsorbed on the AuNP fractals at different concentrations, respectively. The calculation of the intensity ratio (I_{SERS}/I_{RS}) is straightforward from the Raman measurement. N_{bulk} can be calculated assuming bulk melamine density (1.58 gm/cm^3), and illuminated volume (laser beam area x signal collection depth) during the measurement. Here, a signal collection depth of 0.1 mm was assumed for 633 nm laser on melamine powder, while the laser beam area was ~12.5 μm^2. The calculation of N_{ads} is tricky and requires simplifying assumptions. From the given concentration of melamine in the 30 μL water volume used to disperse the analyte on the AuNP fractals, an estimate of number of melamine molecules per unit volume is possible assuming complete and uniform
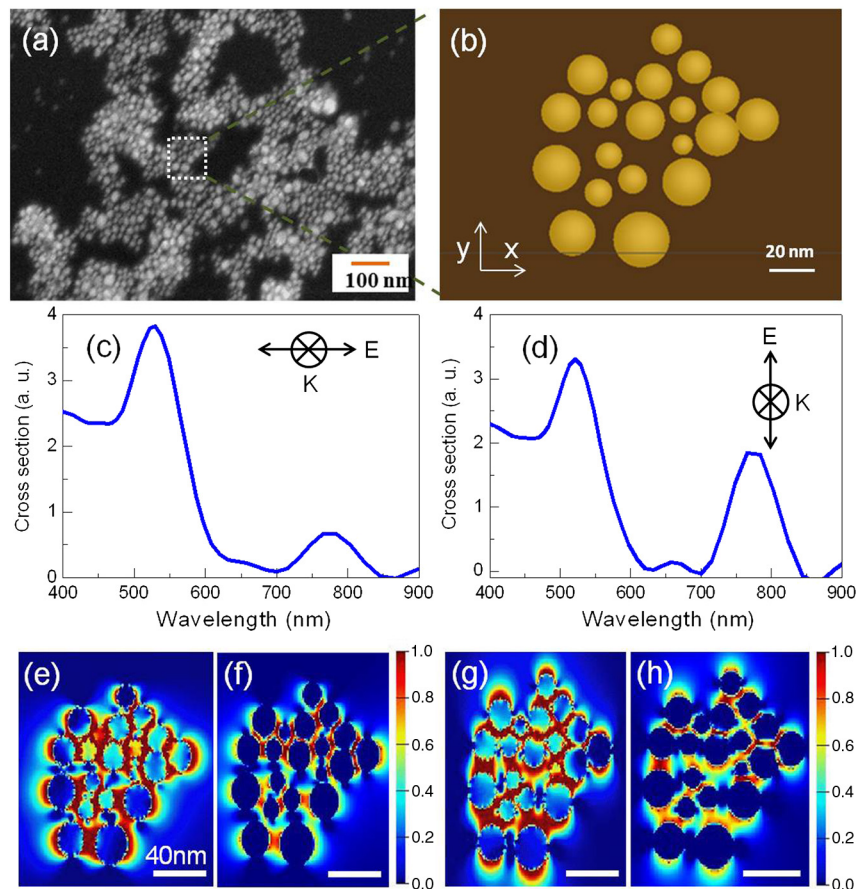
Fig. 6 Numerical simulations using FDTD of the AuNP distribution post 10 ppm melamine exposure assuming surrounding medium index of 1.0. (a) Representative SEM image of the AuNP agglomeration. (b) A model replica of the AuNP distribution, from a selected area of the SEM, for use in the FDTD software. Calculated extinction spectra of the model AuNP distribution [as shown in (b)] with (c) horizontal and (d) vertical incident electric field ($\bar{E}$) polarization. Plasmon electric field mapping on the AuNP distribution with horizontal $\bar{E}$ polarization of (e) 525 and (f) 633 nm excitation, and with vertical $\bar{E}$ polarization of (g) 525 and (h) 633 nm excitation. The wave propagation vector K is perpendicular to the plane of the paper. Same scale bars for (e) to (h).

dispersion on the substrate surface. Under such assumptions and approximation, the EFs were calculated to be 4.9×10^4, 8.5×10^4, 2×10^5, 3.2×10^5, and 1.4×10^6 for the AuNP fractals with $M_c = 10, 5, 1, 0.5$, and 0.1 ppm, respectively. If we assume the SERS signal originating only from the AuNPs, and not from melamine adsorbed on silicon, then the above EF will increase following a decreased N_{ads} on the AuNPs only.

In order to determine why the melamine detection was possible, even without functionalization of the AuNPs, the FDTD simulations (Figs. 6 and 7) were carried out. The presentation of the FDTD results begins with a representative SEM image of a given AuNP distribution. A replica, in size and density, of a section of this AuNP distribution is constructed theoretically. This AuNP distribution model when imported into the FDTD software, the optical extinction spectrum could be calculated. This spectrum will show the surface plasmon absorption peaks of the AuNP distribution at specific wavelengths. A single peak for individual unagglomerated AuNP and two or more peaks for agglomerated AuNPs will be obtained under orthogonal polarization directions (x, y) of the electric field (E) of the incident light. Next, the software scans the replica of the AuNP distribution, constructed previously, with incident light wavelength in resonance with that of the surface plasmon absorption peaks obtained in the respective extinction spectrum. This would result in the surface plasmon E-field mapping of the entire AuNP distribution. This procedure is repeated for the two polarization directions (x, y) and with either one or two wavelengths depending on the respective surface plasmon absorption peaks calculated. In addition, the E-field mapping of the AuNP distribution was also performed with incident wavelength of 633 nm that was used for the Raman measurement.

Figures 6 and 7 contain comparative FDTD optical simulations of the AuNP distribution that were used to detect melamine. A representative SEM image (x, y) of highly agglomerated AuNPs $(M_c = 10$ ppm) [Fig. 6(a)] was used to create exact theoretical replica [Fig. 6(b)] that yielded the extinction spectra (scattering cross-section) using two perpendicular polarizations $(Ex$ and $Ey)$ of the electric field of the incident light [Fig. 6(c) and 6(d)] propagating along the z-direction. The extinction spectra showed double peaks at 525 and ~770 nm (agglomerated AuNPs surface plasmon) [Fig. 6(c) and 6(d)]. Such double peaks in the spectra are present even for the 0.1 ppm melamine exposed AuNPs showing weak agglomeration. Surface plasmon maps of the AuNP distribution shows stronger E-field distribution under 525 nm excitation than under 633 nm, under both vertical [Ex, Fig. 6(e) and 6(f)] and horizontal polarization [Ey, Fig. 6(g) and 6(h)]. This is due to the lower surface plasmon absorption at 633 nm [Fig. 6(c) and 6(d)].

The same presentation scheme was maintained for the case of 0.1 ppm exposed AuNPs (Fig. 7). Since the FDTD calculations
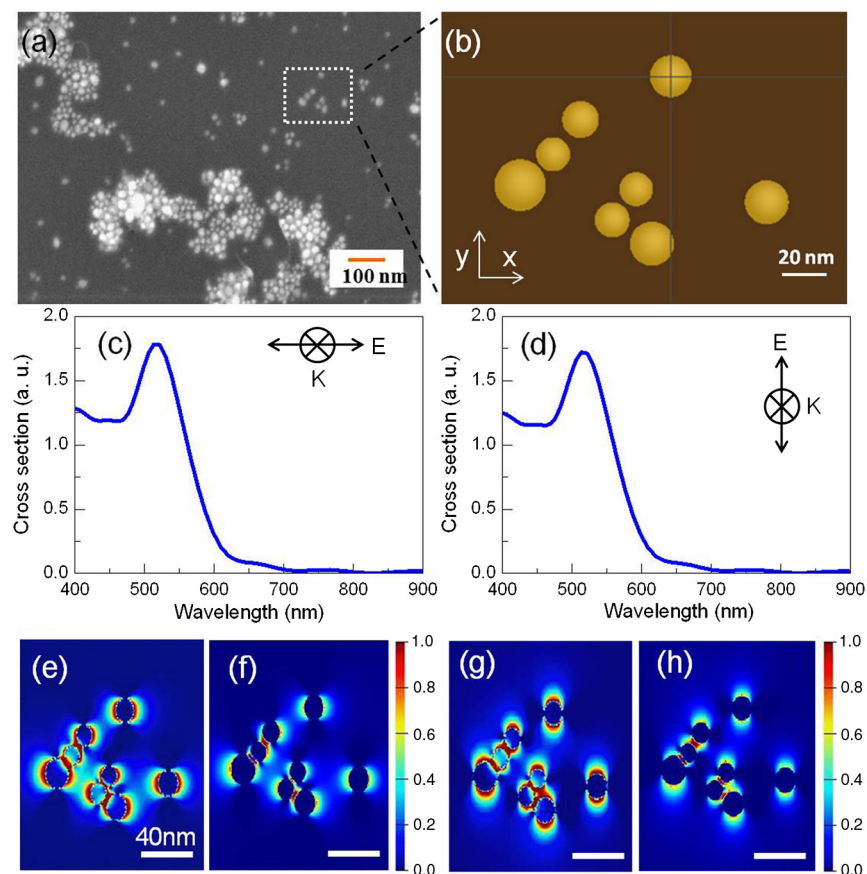
Fig. 7 Numerical simulations using FDTD of the AuNP distribution post 0.1 ppm melamine exposure assuming surrounding medium index of 1.0. (a) Representative SEM image of the AuNP distribution. (b) A model replica of the AuNP distribution, from a selected area of the SEM, for use in the FDTD software. Calculated extinction spectra of the model AuNP distribution [as shown in (b)] with (c) horizontal and (d) vertical incident electric field ($\bar{E}$) polarization. Plasmon electric field mapping on the AuNP distribution with horizontal $\bar{E}$ polarization of (e) 525 and (f) 633 nm excitation, and with vertical $\bar{E}$ polarization of (g) 525 and (h) 633 nm excitation. The wave propagation vector K is perpendicular to the plane of the paper. Same scale bars for (e) to (h).

depend on the density and the size of the AuNPs, the chosen area of the SEM [Fig. 7(a)] and its theoretical replica [Fig. 7(b)] roughly had similar AuNP distribution (particles/μm^2) for 0 [Fig. 2(a)] and 0.1 ppm [Fig. 2(d)] melamine exposure. This is assumed for simplicity and no loss of technicality. In this case, only one scattering peak (as expected for mostly individual AuNPs at a low spatial density) is observed at ~525 nm [Fig. 7(c) and 7(d)] for both Ex and Ey. The plasmonic E-field map, at 525 and 633 nm, shows weak local plasmons centered around the individual AuNPs under both polarization conditions [Fig. 7(e) to 7(h)].

SERS-aided detection is a plasmonic phenomenon where the local electric field at the analyte site dictates σ_{SERS}.[41] In other words, a strong plasmon [red color in Figs. 6(e) to 6(h), and 7(e) to 7(h)] field coverage of the detector surface (per unit area) would increase the scattered intensity (I_{676}) to detectable limits. The simulated plasmon mapping shown in Figs. 6(e) to 6(h), and 7(e) to 7(h) was obtained assuming spherical AuNPs. However, the TEM results [Fig. 1(c)] clearly showed that the AuNPs distribution contained triangular and hexagonal AuNPs with sharp corners and edges. The shape dependence of SERS, reported earlier, indicate that though spheres are excellent model systems for simulations, the maximum enhancement comes

from aggregates or fractal like structures of ellipsoids.[42] However, even the spherical model approximation for the FDTD calculations gives us a lower bound for the plasmon field distributions. In reality, the electric fields would be higher considering the triangular or hexagonal AuNPs. The other usefulness of the FDTD calculations is that it can predict the absorption frequencies for the clusters/fractals under consideration. While a sphere can resonate at one particular frequency (or wavelength), a spheroid can resonate at three different frequencies and a random fractal may resonate at any given frequency over a broad spectral region.[43] These localized resonances in fractals increase in number from visible to near-IR increasing the probability of obtaining higher enhancement factors in SERS. Under the given experimental conditions, higher M_c (10 to 1 ppm) could agglomerate the AuNPs so that a strong plasmon field with wide coverage [Fig. 6(e) to 6(h)] could be obtained over the detector surface. Such area of strong plasmon field decreases with decreasing M_c. This is why I_{676} decreases with decreasing M_c [Fig. 3(a) to 3(e)]. At $M_c = 0.1$ ppm, such AuNP clusters still remained so that we could detect the melamine signal, though weak, quite consistently [Fig. 3(e)]. However, for AuNPs that did not agglomerate when $M_c = 0.1$ [Fig. 7(b)] or 0 ppm [Fig. 2(a)], the plasmon field, with an
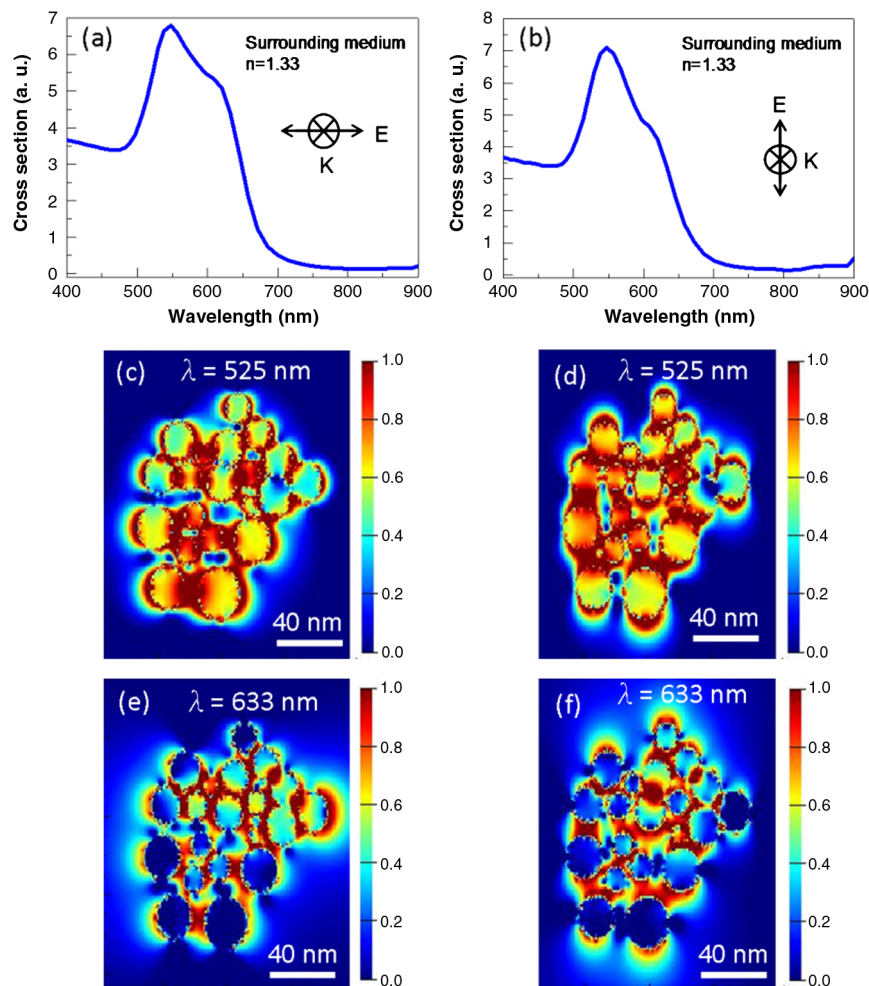
Fig. 8 FDTD simulations of the AuNP distribution post 10 ppm melamine exposure [as shown in Fig. 6(b)] with surrounding medium index of 1.33.Calculated extinction spectra with (a) horizontal and (b) vertical incident electric field ($\bar{E}$) polarization. Plasmon electric field mapping on the AuNP distribution with (c) horizontal and (d) vertical $\bar{E}$ polarization of 525 nm, and (e) horizontal and (f) vertical $\bar{E}$ polarization of 633 nm excitation. The wave propagation vector K is perpendicular to the plane of the paper.

absorption peak at ~525 nm [Fig. 7(c) and 7(d)], is weak with low surface coverage [Fig. 7(e) to 7(h)] and hence detection was either difficult or not possible at all. The scarce presence of red color in Fig. 7(e) to 7(h) only indicates a lower probability of scattering and greater degree of uncertainty in measurement under both 525 or 633 nm excitation.

However, the calculated surface plasmon absorption of the AuNP distribution, though strong around 525 nm, was weak at the Raman measurement wavelength of 633 nm [Fig. 6(c) to 6(d); Fig. 7(c) to 7(d)]. Within our experimental rage of M_c (10 to 0.1 ppm), the index of the surrounding medium was assumed to be 1.0 in our FDTD calculations shown in Figs. 6 and 7. If we take into account the presence of melamine within the fractals, then the effective index would be higher than 1.0, depending on its volume fraction, scaling with M_c. Although the exact index cannot be calculated, due to the uncertain coverage, we performed the FDTD calculations with higher representative index of 1.33 under 525 and 633 nm excitation. The results, irrespective of the AuNP distribution and incident $\bar{E}$ field polarization, show an increasing plasmon absorption band around ~600 nm (Figs. 8 and 9) where the actual Raman measurements were performed. Usual red shift, towards higher wavelength, of the absorption bands are expected and observed

with increasing index as reported before.[44,45] Although the 525 nm band was still the strongest [Figs. 8(a), 8(b), 9(a), and 9(b)], the plasmon field distribution at 525 [Fig. 8(c) and 8(d)] and 633 nm [Fig. 8(e) to 8(f)] excitation was markedly improved at background index of 1.33 compared to calculations done with background index of 1.0 for each excitation wavelength [Fig. 6(e) and 6(h)]. These results can now explain why we could still detect melamine with high sensitivity at 633 nm. The limit of detection would have been lower if we could measure at 525 nm because of the strongest surface plasmon absorption at that wavelength in the given AuNP fractal distribution. In short, we demonstrate how 100 ppb of melamine could be reproducibly detected on AuNP-fractals that creates a given plasmon field distribution as shown in Fig. 6(e) to 6(h) and Fig. 8(c) and 8(f).

To confirm, whether the strategy will still work when we extract melamine from a milk colloid, we performed similar SERS measurements with samples extracted from real contaminated milk. The extract contained melamine suspended in the liquid of milk with its proteins removed. Figure 10 shows SERS data of milk extracts containing different M_c. Experimental designs and conditions remaining the same, similar results were obtained with the I_{676} diminishing in intensity
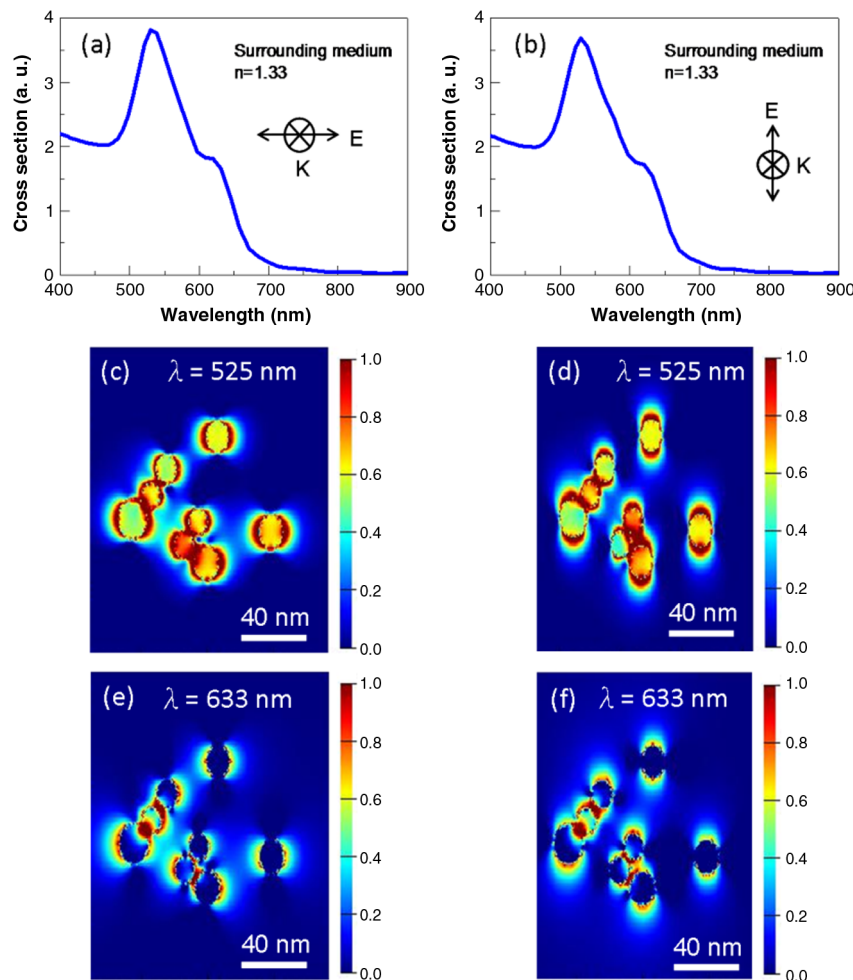
Fig. 9 FDTD simulations of the AuNP distribution post 0.1 ppm melamine exposure [as shown in Fig. 7(b)] with surrounding medium index of 1.33. Calculated extinction spectra with (a) horizontal and (b) vertical incident electric field ($\bar{E}$) polarization. Plasmon electric field mapping on the AuNP distribution with (c) horizontal and (d) vertical $\bar{E}$ polarization of 525 nm, and (e) horizontal and (f) vertical $\bar{E}$ polarization of 633 nm excitation. The wave propagation vector K is perpendicular to the plane of the paper.
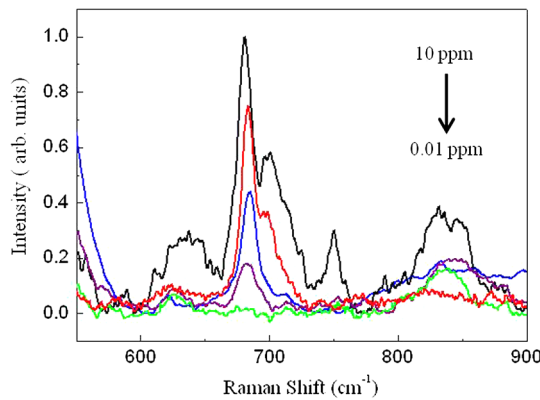
Fig. 10 Surface-enhanced Raman scattering data of melamine containing milk extract on Au fractals. Normalized (to I_{676}) SERS spectra of melamine containing milk extract with $M_c = 10$, 5, 1, 0.1, and 0.01 ppm, arranged in order.
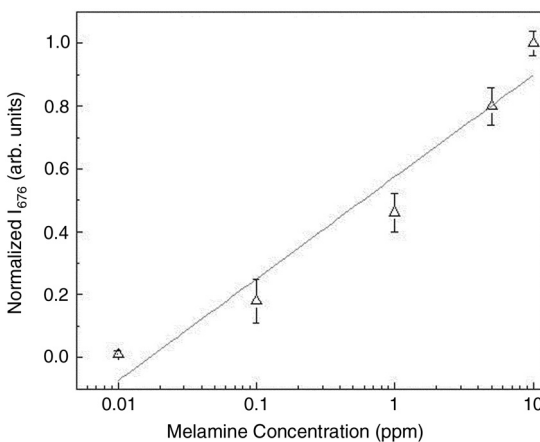
Fig. 11 Variation of the normalized intensity of the 676 cm^{-1} line of melamine Raman spectrum as a function of melamine concentration (in milk extract, Fig. 10) when dispersed on gold fractals (SERS). A linear fit to the data is also shown. The R^2 value of the fit is 0.93. The slope of the line is an indication of the sensitivity of the measurements.

with a lowering of M_c. Some background signals from the Si substrate and remnant milk components could be seen as well. The variation of the normalized I_{676} as a function of M_c (in milk extract) is shown in Fig. 11 whose slope is indicative of the sensitivity of detection in the studied concentration range. Here also, we could detect up to 100 ppb of melamine in milk from the feature at 676 cm^{-1} in the SERS spectra (Fig. 10). Lowering M_c to 10 ppb resulted in virtually no signal (I_{676}) (Fig. 10). However, we could say, with confidence, that at least 100 ppb of melamine could be detected with a simple AuNPs distribution, with particle size ~20 to 30 nm, which demonstrated a plasmon field as shown in Figs. 6(e) to 6(h) and 8(c) and 8(f).

4 Conclusions

Presence of melamine was detected in raw milk by surface-enhanced Raman scattering using silicon substrates dispersed with unmodified 30 nm AuNPs. Melamine was found to agglomerate the AuNPs with as-dispersed densities of 300 AuNPs/μm^2, to predominantly 2-D clusters with densities of ~2100 AuNPs/μm^2 (at 10 ppm concentration), that helped to generate a strong plasmonic field under illumination. The

absorption and plasmon field strength of the agglomerated AuNPs were simulated by FDTD method. The optical simulations helped to qualitatively estimate the plasmon distribution to enable melamine detection to a limit of 100 ppb. Melamine containing milk extracts when applied to these unmodified AuNPs coated surfaces yielded strong Raman signals at 676 cm^{-1} indicating the presence of melamine. The absence of the AuNPs on the same substrates yielded no Raman signals under similar experimental conditions. A limit of detection of 100 ppb could be reproducibly obtained in this technique.

References

1. B. M. Kuehn, "Melamine scandals highlight hazards of increasingly globalized food chain," *J. Am. Med. Assoc.* **301**(5), 473–475 (2009).
2. C. A. Haller, "Made in China," *J. Med. Toxicol.* **4**(2), 141–142 (2008).
3. Z. C. Y. Chan and W. F. Lai, "Revisiting the melamine contamination event in China: implications for ethics in food technology," *Trends Food Sci. Technol.* **20**(8), 366–373 (2009).
4. R. Reimschuessel and B. Puschner, "Melamine toxicity-stones vs. crystals," *J. Med. Toxicol.* **6**(4), 468–469 (2010).
5. A. Ranganathan, V. R. Pedireddi, and C. N. R. Rao, "Hydrothermal synthesis of organic channel structures: 1:1 hydrogen-bonded adducts of melamine with cyanuric and trithiocyanuric acids," *J. Am. Chem. Soc.* **121**(8), 1752–1753 (1999).
6. T. K. Chakraborty, S. Tapadar, and S. K. Kumar, "Cyclic trimer of 5-(aminomethyl)-2-furancarboxylic acid as a novel synthetic receptor for carboxylate recognition," *Tetrahedron Lett.* **43**(7), 1317–1320 (2002).
7. A. K. C. Hau, T. H. Kwan, and P. K. T. Li, "Melamine toxicity and the kidney," *J. Am. Soc. Nephrol.* **20**(2), 245–250 (2009).
8. World Health Organization, "Melamine and Cyanuric Acid: Toxicity, preliminary risk assessment and guidance on levels in food," (25 September 2008), http://advocatingbreastfeeding.wordpress.com/2008/09/30/who-melamine-and-cyanuric-acid-toxicity-preliminary-risk-assessment-and-guidance-on-levels-in-food-for-everyone/.
9. S. Ehling, S. Tefera, and I. P. Ho, "High-performance liquid chromatographic method for the simultaneous detection of the adulteration of cereal flours with melamine and related triazine by-products ammeline, ammelide, and cyanuric acid," *Food Addit. Contam.* **24**(12), 1319–1325 (2007).
10. R. A. Yokley et al., "Analytical method for the determination of cyromazine and melamine residues in soil using LC-UV and GC-MSD," *J. Agric. Food Chem.* **48**(8), 3352–3358 (2000).
11. M. S. Filigenzi et al., "The determination of melamine in muscle tissue by liquid chromatography/tandem mass spectrometry," *Rapid Commun. Mass Spectrom.* **21**(24), 4027–4032 (2007).
12. T. Sugita et al., "Determination of melamine and three hydrolytic products by liquid chromatography," *Bull. Environ. Contam. Toxicol.* **44**(4), 567–571 (1990).
13. J. P. Toth and P. C. Bardalaye, "Capillary gas chromatographic separation and mass spectrometric detection of cyromazine and its metabolite melamine," *J. Chromatograph. A* **408**, 335–340 (1987).
14. C. C. Liu et al., "Detection of melamine in a human renal uric acid stone by matrix-assisted laser desorption/ionization time-of-flight mass spectrometry (MALDI-TOF MS)," *Clin. Chim. Acta.* **413**(19–20), 1689–1695 (2012).
15. H. W. Tang et al., "Analysis of melamine cyanurate in urine using matrix-assisted laser desorption/ionization mass spectrometry," *Anal. Chem.* **81**(9), 3676–3682 (2009).

16. L. Zhu et al., "Rapid detection of melamine in untreated milk and wheat gluten by ultrasound-assisted extractive electrospray ionization mass spectrometry (EESI-MS)," *Chem. Commun.* (5), 559–561(2009).

17. E. A. E. Garber, "Detection of melamine using commercial enzyme-linked immunosorbent assay technology," *J. Food Prot.* **71**(3), 590–594 (2008).

18. L. J. Mauer et al., "Melamine detection in infant formula powder using near- and mid-infrared spectroscopy," *J. Agric. Food Chem.* **57**(10), 3974–3980 (2009).

19. R. K. Bera and C. R. Raj, "Naked eye sensing of melamine using rationally tailored gold nanoparticles: hydrogen-bonding and charge-transfer recognition," *Analyst* **136**(8), 1644–1648 (2011).

20. B. Roy, A. Saha, and A. K. Nandi, "Melamine sensing through riboflavin stabilized gold nanoparticles," *Analyst* **136**(1), 67–70 (2011).

21. C. P. Han and H. B. Li, "Visual detection of melamine in infant formula at 0.1 ppm level based on silver nanoparticles," *Analyst* **135**(3), 583–588 (2010).

22. K. L. Ai, Y. L. Liu, and L. H. Lu, "Hydrogen-bonding recognition-induced color change of gold nanoparticles for visual detection of melamine in raw milk and infant formula," *J. Am. Chem. Soc.* **131**(27), 9496–9497 (2009).

23. N. Ding et al., "Colorimetric determination of melamine in dairy products by Fe3O4 magnetic nanoparticles–H2O2–ABTS detection system," *Anal. Chem.* **82**(13), 5897–5899 (2010).

24. L. He et al., "A new approach to measure melamine, cyanuric acid, and melamine cyanurate using surface enhanced Raman spectroscopy coupled with gold nanosubstrates," *Sens. Instrumen. Food Qual.* **2**(1), 66–71 (2008).

25. Y. L. Liu et al., "Potential of Raman spectroscopy and imaging methods for rapid and routine screening of the presence of melamine in animal feed and foods," *Appl. Spectrosc.* **63**(4), 477–480 (2009).

26. S. Okazaki et al., "Rapid nondestructive screening for melamine in dried milk by Raman spectroscopy," *Forensic Toxicol.* **27**(2), 94–97 (2009).

27. Y. Cheng et al., "Screening melamine adulterant in milk powder with laser Raman spectrometry," *J. Food Compos. Anal.* **23**(2), 199–202 (2010).

28. J. Kimling et al., "Turkevich method for gold nanoparticle synthesis revisited," *J. Phys. Chem. B* **110**(32), 15700–15707 (2006).

29. J. Turkevich et al., "A study of the nucleation and growth in the synthesis of colloidal gold," *Discuss. Faraday Soc.* **11**(4), 55–75 (1951).

30. H. Huang et al., "Surface-enhanced Raman spectra of melamine and other chemicals using a 1550 nm (retina-safe) laser," *J. Raman Spectrosc.* **43**(6), 701–705 (2012).

31. X. F. Zhang et al., "Detection of melamine in liquid milk using surface-enhanced Raman scattering spectroscopy," *J. Raman Spectrosc.* **41**(12), 1655–1660 (2010).

32. D. A. Weitz, M. Y. Lin, and C. J. Sandroff, "Colloidal aggregation revisited: new insights based on fractal structure and surface-enhanced Raman scattering," *Surf. Sci.* **158**(1–3), 147–164 (1985).

33. H. Feilchenfeld and O. Siiman, "Adsorption and aggregation kinetics and its fractal description for chromate, molybdate, and tungstate ions on colloidal silver from surface Raman spectra," *J. Phys. Chem.* **90**(19), 4590–4599 (1986).

34. O. Siiman and H. Feilchenfeld, "Internal fractal structure of aggregates of silver particles and its consequences on surface-enhanced Raman scattering intensities," *J. Phys. Chem.* **92**(2), 453–464 (1988).

35. J. GarciaVidal and J. B. Pendry, "Collective theory for surface enhanced Raman scattering," *Phys. Rev. Lett.* **77**(6), 1163–1166 (1996).

36. S. M. Nie and S. R. Emery, "Probing single molecules and single nanoparticles by surface-enhanced Raman scattering," *Science* **275**(5303), 1102–1106 (1997).

37. E. Doering and S. M. Nie, "Single-molecule and single-nanoparticle SERS: examining the roles of surface active sites and chemical enhancement," *J. Phys. Chem. B.* **106**(2), 311–317 (2002).

38. E. C. Le Ru et al., "Surface enhanced Raman scattering enhancement factors: a comprehensive Study," *J. Phys. Chem. C* **111**(37), 13794–13803 (2007).

39. S. Chattopadhyay et al., "Surface-Enhanced Raman Spectroscopy Using Self-Assembled Silver Nanoparticles on Silicon Nanotips," *Chem. Mater.* **17**(3), 553–559 (2005).

40. A. Shalabney et al., "Detailed study of surface-enhanced Raman scattering from metallic nanosculptured thin films and their potential for biosensing," *J. Nanophoton.* **6**(1), 061605 (2012).

41. F. L. Yap et al., "Nanoparticle cluster arrays for high-performance SERS through directed self-assembly on flat substrates and on optical fibers," *ACS Nano.* **6**(3), 2056–2070 (2012).

42. E. J. Zeman and G. C. Schatz, "An accurate electromagnetic theory study of surface enhancement factors for silver, gold, copper, lithium, sodium, aluminum, gallium, indium, zinc, and cadmium," *J. Phys. Chem.* **91**(3), 634–643 (1987).

43. V. A. Shubin et al., "Local electric and magnetic fields in semicontinuous metal films: beyond the quasistatic approximation," *Phys. Rev. B* **62**(16), 11230–11244 (2000).

44. J. J. Mock, D. R. Smith, and S. Schultz, "Local refractive index dependence of plasmon resonance spectra from individual nanoparticles," *Nano Lett.* **3**(4), 485–491 (2003).

45. Y. H. Lee et al., "Refractive index sensitivies of noble metal nanocrystals: the effects of multipolar plasmon resonances and the metal type," *J. Phys. Chem. C* **115**(16), 7997–8004 (2011).